International Journal of Solids and Structures 49 (2012) 3942–3952

Contents lists available at SciVerse ScienceDirect

International Journal of Solids and Structures

journal homepage: www.elsevier.com/locate/ijsolstr

Numerical study of the grain-size dependent Young's modulus and Poisson's ratio of bulk nanocrystalline materials

Tae-Yeon Kim [a,*], John E. Dolbow [b], Eliot Fried [a]

[a] Department of Mechanical Engineering, McGill University, Montréal, Québec, Canada H3A 2K6
[b] Department of Civil and Environmental Engineering, Duke University, Durham, NC 27708, USA

ARTICLE INFO

Article history:
Received 12 June 2012
Received in revised form 13 August 2012
Available online 18 September 2012

Keywords:
Length-scale effects
Grain boundaries
Grain boundary junctions
Finite-element
Continuous–discontinuous Galerkin

ABSTRACT

We present a numerical study of the elastic properties of bulk nanocrystalline materials based on a continuum theory, introduced by Fried and Gurtin (2009), for nanoscale polycrystalline elasticity that captures length-scale effects and accounts for interactions across grain boundaries via interface and junction conditions. The theory involves a balance equation containing fourth-order gradients of the displacement field. A relatively inexpensive, non-conforming finite-element method based on C^0-continuous basis functions is presented. We develop the variational form of the method and establish consistency. The formulation weakly enforces continuity of derivatives of the displacement field across interelement boundaries and stabilization is achieved via Nitsche's method. Based on this approach, numerical studies are performed for a polycrystal subject to an uniaxial deformation. Results indicate that the theory predicts lower Young's modulus for bulk nanocrystalline materials than for conventional coarsely-grained polycrystals. Moreover, as the grain size decreases below a certain threshold, the effective elastic modulus decreases and the effective Poisson's ratio increases. The distribution of the effective stress shows that the theory captures high strain gradients in the vicinity of the grain boundaries and triple junctions.

1. Introduction

A bulk nanocrystalline material is a polycrystal with a grain size of characteristic linear dimension less than 100 nm. Applications of these materials are rapidly growing. For example, nanocrystalline coatings and thin films are applied to protect cutting tools and engineering components from abrasion, erosion, and corrosion (Suryanarayana and Koch, 2000; Tjong and Chen, 2004) and to reduce the friction of bearings and sliding components operating without liquid lubricants (Koch, 2007).

The novel properties of nanocrystalline materials are generally attributed to the high density of grain boundaries and junctions. Due to the very small grain size, a larger number of the atoms lie within grain boundaries and junctions than in conventional (i.e., coarsely-grained) polycrystals. Roughly 25% of the atoms of nanocrystalline materials with a grain size of 10 nm and a grain boundary thickness of about 1 nm are contained in grain boundaries and grain junctions and that percentage increases twofold when the grain size is reduced to 5 nm (Siegel, 1991; Sharma and Ganti, 2003). Grain-size dependence can be somewhat more pronounced for nanocrystalline ceramics (Yeheskel et al., 2005). Strategies that seek to capitalize on these features of nanocrystalline materials have grown significantly over the past decade (Gleiter, 1989, 2000; Suryanarayana and Koch, 2000; Kumar et al., 2003; Tjong and Chen, 2004; Han et al., 2005; Meyers et al., 2006; Dao et al., 2005; Koch, 2007; Ramesh, 2009).

While considerable attention has been and continues to be paid to understanding the inelastic behavior of nanocrystalline materials, relatively little work has been performed on the grain-size dependent elastic properties of polycrystals. The earliest measurements of the Young's modulus for various nanocrystalline materials such as iron (Fe), copper (Cu), and palladium (Pd) reported values substantially lower than those of conventional polycrystals (Gleiter, 1989; Nieman et al., 1991; Fougere et al., 1995; Sanders et al., 1997). Although these low values were later attributed to pores with cracks growing out of them (Fougere et al., 1995; Sanders et al., 1997; Krstic et al., 1993; Shen et al., 1995), subsequent measurements on porosity-free pure cubic nanocrystalline metals revealed reductions of moduli of up to 20% for sufficiently small grains (Gallas and Piermarini, 1991; Tanimoto et al., 1999).

Recently, Fried and Gurtin (2009) introduced a continuum theory for nanoscale polycrystalline elasticity that captures length-scale effects and endows junctions with gradient-energy induced conditions. The theory is aimed at situations that arise before the onset of inelastic processes such as interfacial slip and separation. The purpose of this paper is to explore the elastic properties of nanocrystalline materials based on this theory through the development and application of a relatively inexpensive finite-element method.

* Corresponding author.
E-mail address: tykimsay@gmail.com (T.-Y. Kim).

0020-7683/$ - see front matter © 2012 Elsevier Ltd. All rights reserved.
http://dx.doi.org/10.1016/j.ijsolstr.2012.08.023

Most numerical work on nanocrystalline materials has focused on inelastic behavior. For example, molecular dynamics has been widely used to predict that the primary mechanism responsible for plastic deformation in nanocrystalline metals is grain boundary sliding (Schiotz et al., 1999; Van Swygenhoven and Derlet, 2001; Hasnaoui et al., 2003). While molecular dynamics has been a useful tool in this regard, calculations for samples with experimentally useful sizes and for realistic strain rates are prohibitively expensive. Some numerical work has also been performed on elastic properties of nanocrystalline materials. Bush (1993) used a boundary-element method to study the effective Young's modulus for nanocrystalline palladium. Based on the work of Bush, Kim et al. (1998) presented a similar approach and, in addition, they considered porosity and used the finite-element method. Kim and Bush (1999) developed a phase mixture model consisting of a mixture of crystalline phase, intercrystalline phase (grain boundary, triple line junction, and quadratic node), and pores and investigated the effects of grain size and porosity on the Young's modulus of nanocrystalline materials.

The balance equation arising from the theory of Fried and Gurtin (2009) involves fourth-order partial derivatives. Hence, a standard Galerkin approximation requires C^1-continuous basis functions such that both the displacement field and its first derivatives are continuous. Examples include functions based on Hermite polynomials. While relatively simple to construct on uniform meshes, unstructured meshes present difficulties and certain partitions are not permissible with isoparametric versions of Hermite elements (e.g., Petera and Pittman, 1994). Mixed finite-element methods present a relatively expensive alternative, requiring separate approximations for primary and secondary fields (e.g., Fortin and Brezzi, 1991). While isogeometric analysis (Hughes et al., 2005) circumvents some of these issues, generating B-spline bases that conform to a polycrystalline geometry is not a trivial exercise.

To overcome some of the drawbacks of these traditional methods, we adapt a continuous–discontinuous Galerkin (CDG) method proposed by Engel et al. (2002). This is essentially a non-conforming method — as the basis functions, while continuous, do not lie in the proper space for a strict Galerkin method. Continuity requirements for the derivatives are weakly satisfied by borrowing concepts from discontinuous Galerkin methods, in particular by extending the variational equation to include stabilization terms on interelement boundaries. Engel et al. (2002) applied the method to solve problems involving fourth-order elliptic operators arising from theories for thin beams and plates and strain-gradient elasticity. Moreover, Kim et al. (2007) employed this method to study a fourth-order balance equation arising from a second-gradient theory for fluid flows at small length scales.

In the present paper, we develop a comparable formulation of the second-gradient theory for the study of polycrystalline elasticity. The CDG method we employ here builds upon important concepts from the discontinuous Galerkin literature, in particular those schemes designed for spatial discontinuities. The method we present is closely tied to an approach introduced by Nitsche's (1970) for elliptic and parabolic problems. A similar effort to consistently embed constraints into a weak form was proposed by Babuška (1973). Douglas and Dupont (1976) subsequently augmented Nitsche's method by developing interior penalty methods for linear second-order elliptic and parabolic equations. The work of Baumann (1997) on a discontinuous finite-element method for fluid mechanics also relies on concepts that can be traced back to the work of Nitsche. Detailed descriptions of Nitsche's method are provided by Griebel and Schweitzer (2002), Wriggers and Zavarise (2008), and Annavarapu et al. (2012).

The outline of this paper is as follows. In the next section, we present the system of general balance equations along with interfacial and junction conditions at grain boundaries developed by Fried and Gurtin (2009). In Section 3, the variational formulation for those equations and conditions is described. In Section 4, we introduce the non-conforming variational formulation and discretization with finite elements. In Section 5, results of numerical studies designed to explore the performance of the theory are described. Finally, a summary and concluding remarks are given in Section 6.

2. Governing equations

We work with the generalized balance equations, introduced by Fried and Gurtin (2009), associated with grain boundaries and triple junctions for second-grade nanocrystalline elastic materials undergoing infinitesimal deformations. The theory is based on a nonstandard form of the principle of virtual power pioneered by Gurtin (2001). The principle of virtual power is used as a basic tool in determining the structure of the tractions, grain boundary and junction conditions, and the local force balances. We remark that the theory neglects stresses, such as surface tension, acting within grain boundaries and the free energy of the grain boundaries. The theory also assumes that the displacement field remains continuous across grain boundaries.

We consider a closed polycrystalline body B consisting of N *grains* identified with the closed regions $B_1, B_2, \ldots, B_N$ that occupy:

$$B = B_1 \cup B_2 \cup \cdots B_N. \tag{1}$$

The system

$$\partial B = \partial B_1 \cup \partial B_2 \cup \cdots \partial B_N$$

of *grain boundaries* is assumed to be the union of ∂B. A finite number of smooth surfaces which pairs of grains intersect are called *interfaces* $\mathcal{I}$ and *triple junctions* $\mathcal{J}$ are curves at which three interfaces intersect. *Boundary junctions* $\partial\mathcal{J}$ are curves along which an interface abuts the boundary ∂B. Fig. 1 shows a schematic view of a polycrystal with three grains and internal boundaries including a triple junction. The triple junction $\mathcal{J}$ at which the grain boundaries $\mathcal{I}_1, \mathcal{I}_2$, and $\mathcal{I}_3$ intersect can be defined by

$$\mathcal{J} = \mathcal{I}_1 \cap \mathcal{I}_2 \cap \mathcal{I}_3, \tag{2}$$

and three boundary junctions are defined as

$$\partial\mathcal{J}_1 = \mathcal{I}_1 \cap \partial B, \quad \partial\mathcal{J}_2 = \mathcal{I}_2 \cap \partial B, \quad \partial\mathcal{J}_3 = \mathcal{I}_3 \cap \partial B. \tag{3}$$

Mechanical balances associated with grain boundaries and triple junctions are derived, assuming that

surface stress within the grain boundaries is negligible. (4)

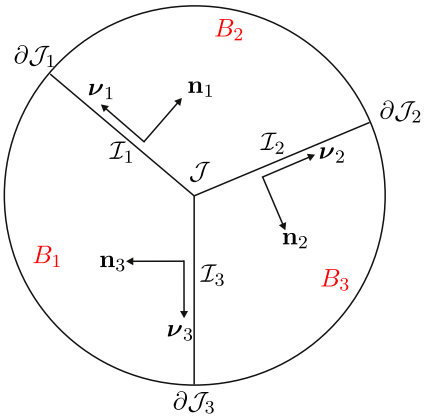

Fig. 1. Schematic view of a polycrystal with three grains (B_1, B_2, B_3), three grain boundaries $(\mathcal{I}_1, \mathcal{I}_2, \mathcal{I}_3)$, three boundary junctions $(\partial\mathcal{J}_1, \partial\mathcal{J}_2, \partial\mathcal{J}_3)$, and a triple junction $\mathcal{J}$ representing the intersection of $\mathcal{I}_1, \mathcal{I}_2$, and $\mathcal{I}_3$. Here, $\mathbf{n}_i$ and $\boldsymbol{\nu}_i$ $(i = 1, 2, 3)$ are unit vectors normal and tangent to $\mathcal{I}_i$, respectively.

In addition, the body B is assumed to be a closed region, and, as is customary,

all test fields $\boldsymbol{\phi}$ are required to be smooth on B. (5)

In view of (4), it seems reasonable to assume that the internal power $\mathcal{W}_{\text{int}}(\boldsymbol{\phi}, R)$ for an arbitrary subregion R of B is obtained by summing over the internal power over the individual grains in R. Then,

$$\mathcal{W}_{\text{int}}(\boldsymbol{\phi}, R) = \int_R (\mathbf{T} : \operatorname{grad}\boldsymbol{\phi} + \mathbf{G} : \nabla \operatorname{curl}\boldsymbol{\phi})\, \mathrm{d}v, \tag{6}$$

where

$$\int_R (\mathbf{T} : \operatorname{grad}\boldsymbol{\phi} + \mathbf{G} : \nabla \operatorname{curl}\boldsymbol{\phi})\, \mathrm{d}v = \sum_{B_n \in R} \int_{B_n} (\mathbf{T} : \operatorname{grad}\boldsymbol{\phi} + \mathbf{G} : \nabla \operatorname{curl}\boldsymbol{\phi})\, \mathrm{d}v, \tag{7}$$

in which $\mathbf{T}$ the Cauchy stress and $\mathbf{T} : \operatorname{grad}\boldsymbol{\phi}$ is the stress power. A second-order tensor-valued *hyperstress* $\mathbf{G}$ is introduced via an internal power expenditure of the form $\mathbf{G} : \nabla \operatorname{curl}\boldsymbol{\phi}$.

In conjunction with the internal power expenditure (6), the corresponding external power expenditure has the form

$$\mathcal{W}_{\text{ext}}(\boldsymbol{\phi}, R) = \int_{\mathcal{S}} \left(\mathbf{t}_{\mathcal{S}} \cdot \boldsymbol{\phi} + \mathbf{m}_{\mathcal{S}} \cdot \frac{\partial \boldsymbol{\phi}}{\partial n} \right) \mathrm{d}a + \int_R \mathbf{b} \cdot \boldsymbol{\phi}\, \mathrm{d}v, \tag{8}$$

in which $\mathbf{t}_{\mathcal{S}}$ and $\mathbf{m}_{\mathcal{S}}$ represent tractions on the bounding surface $\mathcal{S} = \partial R$, while $\mathbf{b}$ *represents the net inertial and noninertial body force* acting within the body. In (8), the term

$$\mathbf{m}_{\mathcal{S}} \cdot \frac{\partial \boldsymbol{\phi}}{\partial n},$$

which is absent from classical theories, is needed to balance the effects of the internal-power term $\mathbf{G} : \nabla \operatorname{curl}\boldsymbol{\phi}$, which involves the second gradient of $\boldsymbol{\phi}$.

Here, rather than work with an arbitrary subregion R, we work with the region B occupied by the body, assuming throughout that ∂B is smooth. The principle of virtual power with $R = B$ and $\mathcal{S} = \partial B$ is therefore based on the requirement that the external and internal powers be balanced as

$$\begin{aligned} &\int_B (\mathbf{T} : \operatorname{grad}\boldsymbol{\phi} + \mathbf{G} : \nabla \operatorname{curl}\boldsymbol{\phi})\, \mathrm{d}v \\ &\quad = \int_{\partial B} \left(\mathbf{t}_{\mathcal{S}} \cdot \boldsymbol{\phi} + \mathbf{m}_{\mathcal{S}} \cdot \frac{\partial \boldsymbol{\phi}}{\partial n} \right) \mathrm{d}a + \int_B \mathbf{b} \cdot \boldsymbol{\phi}\, \mathrm{d}v \end{aligned} \tag{9}$$

for all arbitrary regions B and any choice of the virtual field $\boldsymbol{\phi}$. Unlike test fields $\boldsymbol{\phi}$, which are smooth, the stresses $\mathbf{T}$ and $\mathbf{G}$ generally suffer jump discontinuities across grain boundaries.

Consequences of the virtual power principle and the requirement that the internal power expenditure be frame-indifferent are that:

(i) the classical balance $\operatorname{div}\mathbf{T} + \mathbf{b} = \mathbf{0}$ must be replaced by the internal balance

$$\operatorname{div}\mathbf{T} + \operatorname{curl}\operatorname{div}\mathbf{G} + \mathbf{b} = \mathbf{0}, \quad \text{in each grain interior}, \tag{10}$$

with interfacial conditions

$$\left.\begin{aligned} &[\![\mathbf{T}]\!]\mathbf{n} = \operatorname{div}_{\mathcal{S}}([\![\mathbf{G}]\!]\mathbf{n}\times) - \mathbf{n} \times \operatorname{div}[\![\mathbf{G}]\!], \\ &\mathbf{n} \times [\![\mathbf{G}]\!]\mathbf{n} = \mathbf{0}, \end{aligned}\right\} \quad \text{on } \mathcal{I}, \tag{11}$$

and a triple junction condition

$$\sum_{\iota=1}^{3} \boldsymbol{\nu}_\iota \times [\![\mathbf{G}]\!]_\iota \mathbf{n}_\iota = \mathbf{0} \quad \text{on } \mathcal{J}; \tag{12}$$

(ii) Cauchy's classical condition $\mathbf{t}_{\mathcal{S}} = \mathbf{T}\mathbf{n}$ for the traction across a surface $\mathcal{S}$ with unit normal $\mathbf{n}$ must be replaced by boundary conditions

$$\left.\begin{aligned} &\mathbf{t}_{\mathcal{S}} = \mathbf{T}\mathbf{n} - \operatorname{div}_{\mathcal{S}}(\mathbf{G}\mathbf{n}\times) + \mathbf{n} \times (\operatorname{div}\mathbf{G} + 2H\mathbf{G}\mathbf{n}), \\ &\mathbf{m}_{\mathcal{S}} = \mathbf{G}\mathbf{n} \times \mathbf{n}; \end{aligned}\right\} \quad \text{on } \partial B \setminus \partial\mathcal{J}, \tag{13}$$

and a boundary junction condition

$$\boldsymbol{\nu} \times [\![\mathbf{G}]\!]\mathbf{n} = -\boldsymbol{\nu}_{\mathcal{I}} \times [\![\mathbf{G}]\!]\mathbf{n}_{\mathcal{I}} \quad \text{on } \partial\mathcal{J}, \tag{14}$$

in which $\operatorname{div}_{\mathcal{S}}$ is the divergence operator on $\mathcal{S} = \partial B$ and $H = -\frac{1}{2}\operatorname{div}_{\mathcal{S}}\mathbf{n}$ is the mean curvature of $\mathcal{S}$. In $(11)_1$ and $(13)_1$, $\mathbf{w}\times$ denotes the axial tensor of a vector $\mathbf{w}$, as defined via the requirement that

$$(\mathbf{w}\times)\mathbf{v} = \mathbf{w} \times \mathbf{v}$$

for all vectors $\mathbf{v}$; alternatively, given an orthonormal Cartesian basis $\{\mathbf{e}_1, \mathbf{e}_2, \mathbf{e}_3\}$ and using ϵ_{ijk} to denote the alternating symbol,

$$(\mathbf{w}\times)_{ij} = \mathbf{e}_i \cdot [(\mathbf{w}\times)\mathbf{e}_j] = \epsilon_{ikj} w_k.$$

Consider an interface $\mathcal{I}$ separating grains B_m and B_n, and let

$$R = B_m \cup B_n, \quad R^+ = B_n, \quad R^- = B_m.$$

Further, let $\mathbf{n}$ be the unit normal field on $\mathcal{I}$ directed outward from R^-. Given any field f, $[\![\mathbf{f}]\!]$ is the jump in f across $\mathcal{I}$, i.e.,

$$[\![\mathbf{f}]\!] = f^+ - f^-, \tag{15}$$

where f^+ and f^- are the values of f at the R^+ side and the R^- side of $\mathcal{I}$, respectively.

When supplemented by constitutive equations for the stress and hyperstress, the balance (10) yields a force balance equation. We restrict attention to a homogeneous and isotropic elastic material. In view of the assumption of infinitesimal deformations, Fried and Gurtin (2009) provided in which case the stress $\mathbf{T}$ and hyperstress $\mathbf{G}$ are given by

$$\mathbf{T} = 2\mu\mathbf{E} + \lambda(\operatorname{tr}\mathbf{E})\mathbf{1} \tag{16}$$

and

$$\mathbf{G} = \bar{\mu}(\operatorname{grad}\boldsymbol{\omega} + (\operatorname{grad}\boldsymbol{\omega})^{\top}), \tag{17}$$

where $\mathbf{E}$ is the strain tensor with

$$\mathbf{E} = \frac{1}{2}(\operatorname{grad}\mathbf{u} + (\operatorname{grad}\mathbf{u})^{\top}) \tag{18}$$

for the displacement field $\mathbf{u}$.

Substituting (16) and (17) into (10) yields the force balance equation

$$\mu\Delta\mathbf{u} + (\lambda + \mu)\nabla \operatorname{div}\mathbf{u} + \bar{\mu}\Delta(\nabla \operatorname{div}\mathbf{u} - \Delta\mathbf{u}) + \mathbf{b} = \mathbf{0}, \tag{19}$$

which is non-dimensionalized by introducing a characteristic length scale L and a characteristic displacement U. For convenience, the symbols used in the original dimensional variables are retained, in which case the dimensionless version of (10) reads

$$\Delta\mathbf{u} + \frac{\lambda + \mu}{\mu}\nabla \operatorname{div}\mathbf{u} + \frac{\bar{\mu}}{\mu L^2}\Delta(\nabla \operatorname{div}\mathbf{u} - \Delta\mathbf{u}) + \mathbf{b} = \mathbf{0}. \tag{20}$$

The dimensionless interfacial conditions (11) and boundary conditions (13) consistent with the nondimensionalization leading to (20) are

$$\begin{aligned} &[\![\mathbf{T}']\!]\mathbf{n} = \frac{\bar{\mu}}{\mu L^2}\operatorname{div}_{\mathcal{S}}([\![\mathbf{G}']\!]\mathbf{n}\times) - \frac{\bar{\mu}}{\mu L^2}(\mathbf{n} \times \operatorname{div}[\![\mathbf{G}']\!]), \\ &\mathbf{t}'_{\mathcal{S}} = \mathbf{T}'\mathbf{n} - \frac{\bar{\mu}}{\mu L^2}\operatorname{div}_{\mathcal{S}}(\mathbf{G}'\mathbf{n}\times) + \frac{\bar{\mu}}{\mu L^2}[\mathbf{n} \times (\operatorname{div}\mathbf{G}' + 2H\mathbf{G}'\mathbf{n})], \end{aligned} \tag{21}$$

where $\mathbf{T}' = 2\mathbf{E}_{ij} + \frac{\lambda}{\mu}(\operatorname{tr}\mathbf{E})\mathbf{1}$, $\mathbf{G}' = (\operatorname{grad}\boldsymbol{\omega} + (\operatorname{grad}\boldsymbol{\omega})^{\top})$, and $\mathbf{t}'_{\mathcal{S}} = L\mathbf{t}_{\mathcal{S}}/\mu$. Notice that the dimensionless equations for the remaining conditions are unchanged.

The dimensionless equations result in the parameter:

$$\delta = \frac{\bar{\mu}}{\mu L^2}, \tag{22}$$

where μ is the standard shear modulus, $\bar{\mu}$ is a corresponding gradient modulus that enters the constitutive relation for the hyperstress $\mathbf{G}$, and L might be chosen to coincide with the size of a grain. Importantly, the classical balance equations are recovered from (20) as δ approaches to zero. On the other hand, as δ increases, both the balance equation (20) and interfacial and boundary conditions (21) indicate that the influence of the gradient modulus and the size-dependence of the material properties becomes significant.

3. Variational formulation for a polycrystal

For numerical simulations, we consider a mixed boundary-value problem in which a portion $\mathcal{S}_{\text{free}}$ of $\mathcal{S} = \partial B$ is loaded by tractions $\mathbf{t}_{\mathcal{S}}$ and hypertractions $\mathbf{m}_{\mathcal{S}}$ and the remainder $\mathcal{S}_{\text{fxd}}$ is fixed, in which case

$$\left.\begin{aligned} \mathbf{t}_{\mathcal{S}} &= \mathbf{T}\mathbf{n} - \operatorname{div}_{\mathcal{S}}(\mathbf{G}\mathbf{n}\times) + \mathbf{n}\times(\operatorname{div}\mathbf{G} + 2H\mathbf{G}\mathbf{n}), \\ \mathbf{m}_{\mathcal{S}} &= \mathbf{G}\mathbf{n}\times\mathbf{n} \end{aligned}\right\} \quad \text{on } \mathcal{S}_{\text{free}} \tag{23}$$

and

$$\mathbf{u} = \frac{\partial \mathbf{u}}{\partial n} = \mathbf{0} \quad \text{on } \mathcal{S}_{\text{fxd}}. \tag{24}$$

Consistent with (24), we refer to an arbitrary test field $\tilde{\mathbf{u}}$ as *kinematically admissible* if

$$\tilde{\mathbf{u}} = \frac{\partial \tilde{\mathbf{u}}}{\partial n} = \mathbf{0} \quad \text{on } \mathcal{S}_{\text{fxd}}. \tag{25}$$

Given such a field, we derive the variational formulation of the governing equation (10) for a polycrystal with internal grain boundaries and triple junctions. We emphasize that the stresses $\mathbf{T}$ and $\mathbf{G}$ generally suffer jump discontinuities across grain boundaries. Assume that the displacement field $\mathbf{u}$ is smooth across grain boundaries and the moduli μ, λ, and $\bar{\mu}$ vary smoothly from grain to grain.

With these assumptions, we choose the admissible space $\mathcal{V} \subset H^2(B)$ for the solution field, where $H^m(B)$ denotes the classical Sobolev space of order m. Using the principal of virtual power, Fried and Gurtin (2009) derived the variational formulation with internal conditions that hold across interfaces and at triple junctions. The variational formulation reads: find $\mathbf{u} \in \mathcal{V}$, such that

$$T(\mathbf{u}, \tilde{\mathbf{u}}) = \ell(\tilde{\mathbf{u}}) \quad \forall \tilde{\mathbf{u}} \in \mathcal{V}, \tag{26}$$

where

$$T(\mathbf{u}, \tilde{\mathbf{u}}) = \mathcal{W}_B(\mathbf{u}, \tilde{\mathbf{u}}) - \mathcal{W}_{\mathcal{I}}(\mathbf{u}, \tilde{\mathbf{u}}) - \mathcal{W}_{\mathcal{J}}(\mathbf{u}, \tilde{\mathbf{u}}) - \mathcal{W}_{\partial\mathcal{J}}(\mathbf{u}, \tilde{\mathbf{u}}), \tag{27}$$

$$\mathcal{W}_B(\mathbf{u}, \tilde{\mathbf{u}}) = \int_B (\mathbf{T} : \operatorname{grad}\tilde{\mathbf{u}} + \mathbf{G} : \operatorname{grad}\operatorname{curl}\tilde{\mathbf{u}})\, \mathrm{d}v, \tag{28}$$

$$\begin{aligned} \mathcal{W}_{\mathcal{I}}(\mathbf{u}, \tilde{\mathbf{u}}) = \int_{\mathcal{I}} &(\llbracket\mathbf{T}\rrbracket\mathbf{n} - \operatorname{div}_{\mathcal{S}}(\llbracket\mathbf{G}\rrbracket\mathbf{n}\times) + 2H\mathbf{n}\times\llbracket\mathbf{G}\rrbracket\mathbf{n} \\ &+ \mathbf{n}\times\operatorname{div}\llbracket\mathbf{G}\rrbracket)\cdot\tilde{\mathbf{u}}\, \mathrm{d}a - \int_{\mathcal{I}} (\mathbf{n}\times\llbracket\mathbf{G}\rrbracket\mathbf{n})\cdot\frac{\partial\tilde{\mathbf{u}}}{\partial n}\, \mathrm{d}a, \end{aligned} \tag{29}$$

$$\mathcal{W}_{\mathcal{J}}(\mathbf{u}, \tilde{\mathbf{u}}) = \sum_{\iota=1}^{3} \int_{\mathcal{J}} (\boldsymbol{\nu}_\iota \times \llbracket\mathbf{G}\rrbracket\mathbf{n}_\iota)\cdot\tilde{\mathbf{u}}\, \mathrm{d}s, \tag{30}$$

$$\mathcal{W}_{\partial\mathcal{J}}(\mathbf{u}^h, \tilde{\mathbf{u}}^h) = \int_{\partial\mathcal{J}} (\boldsymbol{\nu}\times\llbracket\mathbf{G}\rrbracket\mathbf{n} + \boldsymbol{\nu}_{\mathcal{I}}\times\llbracket\mathbf{G}\rrbracket\mathbf{n}_{\mathcal{I}})\cdot\tilde{\mathbf{u}}\, \mathrm{d}s, \tag{31}$$

and

$$\ell(\tilde{\mathbf{u}}) = \int_{\mathcal{S}_{\text{free}}} \mathbf{t}_{\mathcal{S}}\cdot\tilde{\mathbf{u}} + \mathbf{m}_{\mathcal{S}}\cdot\frac{\partial\tilde{\mathbf{u}}}{\partial n}\, \mathrm{d}a. \tag{32}$$

4. Finite-element discretization

We introduce our numerical formulation based on the nonconforming method proposed by Engel et al. (2002). In this approach, the basis functions are C^0-continuous — so that their first and higher-order derivatives are discontinuous. Continuity of the first and higher-order derivatives is weakly enforced by adding weighted residual terms to the variational equation on element boundaries and invoking stabilization techniques. The number of unknowns per element arising for this method is considerably fewer than for alternatives based on traditional strategies such as C^1-continuous basis functions. Hereafter, to avoid confusion with interfaces between grain boundaries, the term *element interior boundaries* is used to describe interelement boundaries.

We use a Galerkin method to approximate the solution to (26) and state the weak form of the variational problem in terms of finite-dimensional spaces $\mathcal{V}^h$. We use a nonconforming method where $\mathcal{V}^h$ is not a subspace of $\mathcal{V}$. To construct the bases, we consider a regular finite-element partition $\mathcal{Q}^h$ for B as defined via

$$\mathcal{Q}^h = \bigcup_{n=1}^{N} \mathcal{Q}_n^h,$$

where N is the number of grains and the finite-element partition $\mathcal{Q}_n^h$ for each grain B_n is constructed as

$$\mathcal{Q}_n^h = \bigcup_{e=1}^{M_n} \mathcal{Q}_e,$$

with an element $\mathcal{Q}_e$ and M_n the total number of elements in the mesh of B_n. Hence, the total number of elements M for B is the sum of all the elements in grains — i.e., $M = \sum_{n=1}^{N} M_n$ and $\mathcal{Q}^h \approx B$.

We choose approximation functions that are continuous on the entire domain but discontinuous in first and higher-order derivatives across element interior boundaries. Further, we consider element interiors $\tilde{\mathcal{Q}}$ defined via

$$\tilde{\mathcal{Q}} = \bigcup_{e=1}^{M} \mathcal{Q}_e. \tag{33}$$

The union $\tilde{\Gamma}$ of element interior boundaries is expressed as

$$\tilde{\Gamma} = \bigcup_{i=1}^{N_i} \Gamma_i, \tag{34}$$

where N_i denotes the number of element interior boundaries. In two dimensions, these refer only to those element edges that are shared by two spatially adjacent elements, and do not include edges along the physical boundary ∂B.

The jump across element interior boundaries is also defined as in (15). The average $\langle\!\langle \mathbf{f} \rangle\!\rangle$ of f across element interior boundaries is defined as

$$\langle\!\langle \mathbf{f} \rangle\!\rangle = \frac{1}{2}(f^+ + f^-). \tag{35}$$

From the definitions of the jump and average operators, we have the useful identity

$$\llbracket fg \rrbracket = \llbracket \mathbf{f} \rrbracket \langle\!\langle g \rangle\!\rangle + \langle\!\langle f \rangle\!\rangle \llbracket g \rrbracket. \tag{36}$$

The method we propose to approximate the solution to the force balance equation (10) can then be stated as: find $\mathbf{u}^h \in \mathcal{V}^h$, such that

$$T_{cd}(\mathbf{u}^h, \tilde{\mathbf{u}}^h) = \ell_{cd}(\tilde{\mathbf{u}}^h), \quad \forall \tilde{\mathbf{u}}^h \in \mathcal{V}^h, \tag{37}$$

where

$$T_{cd}(\mathbf{u}^h,\tilde{\mathbf{u}}^h)=\mathcal{W}_B(\mathbf{u}^h,\tilde{\mathbf{u}}^h)-\mathcal{W}_{\mathcal{I}}(\mathbf{u}^h,\tilde{\mathbf{u}}^h)-\mathcal{W}_{\mathcal{J}}(\mathbf{u}^h,\tilde{\mathbf{u}}^h)-\mathcal{W}_{\partial\mathcal{J}}(\mathbf{u}^h,\tilde{\mathbf{u}}^h), \tag{38}$$

$$\begin{aligned}\mathcal{W}_B(\mathbf{u}^h,\tilde{\mathbf{u}}^h)=&\int_{\tilde{\mathcal{Q}}}(\mathbf{T}^h:\operatorname{grad}\tilde{\mathbf{u}}^h+\mathbf{G}^h:\operatorname{grad}\operatorname{curl}\tilde{\mathbf{u}}^h)\,\mathrm{d}v\\&-\int_{\tilde{\Gamma}}\langle\!\langle\tilde{\mathbf{G}}^h\mathbf{n}\rangle\!\rangle\cdot[\![\operatorname{curl}\mathbf{u}^h]\!]\,\mathrm{d}a-\int_{\tilde{\Gamma}}[\![\operatorname{curl}\tilde{\mathbf{u}}^h]\!]\cdot\langle\!\langle\mathbf{G}^h\mathbf{n}\rangle\!\rangle\,\mathrm{d}a\\&+\tau_i\int_{\tilde{\Gamma}}[\![\operatorname{curl}\tilde{\mathbf{u}}^h]\!]\cdot[\![\operatorname{curl}\mathbf{u}^h]\!]\,\mathrm{d}a+\tau_g\int_{\mathcal{I}}[\![\tilde{\mathbf{u}}^h]\!]\cdot[\![\mathbf{u}^h]\!]\,\mathrm{d}a,\end{aligned} \tag{39}$$

$$\begin{aligned}\mathcal{W}_{\mathcal{I}}(\mathbf{u}^h,\tilde{\mathbf{u}}^h)=&\int_{\mathcal{I}}([\![\mathbf{T}^h]\!]\mathbf{n}-\operatorname{div}_{\mathcal{S}}([\![\mathbf{G}^h]\!]\mathbf{n}\times)+2H\mathbf{n}\times[\![\mathbf{G}^h]\!]\mathbf{n}\\&+\mathbf{n}\times\operatorname{div}[\![\mathbf{G}^h]\!])\cdot\tilde{\mathbf{u}}^h\,\mathrm{d}a-\int_{\mathcal{I}}(\mathbf{n}\times[\![\mathbf{G}^h]\!]\mathbf{n})\cdot\frac{\partial\tilde{\mathbf{u}}^h}{\partial n}\,\mathrm{d}a,\end{aligned} \tag{40}$$

$$\mathcal{W}_{\mathcal{J}}(\mathbf{u}^h,\tilde{\mathbf{u}}^h)=\sum_{\iota=1}^{3}\int_{\mathcal{J}}(\boldsymbol{\nu}_\iota\times[\![\mathbf{G}^h]\!]\mathbf{n}_\iota)\cdot\tilde{\mathbf{u}}^h\,\mathrm{d}s, \tag{41}$$

$$\mathcal{W}_{\partial\mathcal{J}}(\mathbf{u}^h,\tilde{\mathbf{u}}^h)=\int_{\partial\mathcal{J}}(\boldsymbol{\nu}\times[\![\mathbf{G}^h]\!]\mathbf{n}+\boldsymbol{\nu}_{\mathcal{I}}\times[\![\mathbf{G}^h]\!]\mathbf{n}_{\mathcal{I}})\cdot\tilde{\mathbf{u}}\,\mathrm{d}s, \tag{42}$$

and

$$\ell_{cd}(\tilde{\mathbf{u}}^h)=\int_{\mathcal{S}_{\text{free}}}\left(\mathbf{t}_{\mathcal{S}}\cdot\tilde{\mathbf{u}}^h+\mathbf{m}_{\mathcal{S}}\cdot\frac{\partial\tilde{\mathbf{u}}^h}{\partial n}\right)\mathrm{d}a. \tag{43}$$

In (39), τ_i and τ_g denote the stabilization parameters for element interior boundaries and grain boundaries, respectively. The basic structure of $\mathcal{W}_B$ follows from Nitsche's (1970) method for enforcing constraints on element interfaces. $\mathcal{W}_{\mathcal{I}}$, $\mathcal{W}_{\mathcal{J}}$, and $\mathcal{W}_{\partial\mathcal{J}}$ represent jump conditions at grain boundaries, triple junctions, and boundary junctions, respectively.

4.1. Consistency

The consistency of the method is derived through successive application of the divergence theorem to (37). Using the equality (36), we derive

$$\begin{aligned}\int_{\tilde{\mathcal{Q}}}\mathbf{T}^h:\operatorname{grad}\tilde{\mathbf{u}}^h\,\mathrm{d}v=&-\int_{\tilde{\mathcal{Q}}}\operatorname{div}\mathbf{T}^h\cdot\tilde{\mathbf{u}}^h\,\mathrm{d}v+\int_{\mathcal{S}}\mathbf{T}^h\mathbf{n}\cdot\tilde{\mathbf{u}}^h\,\mathrm{d}a\\&+\int_{\tilde{\Gamma}}([\![\mathbf{T}^h\mathbf{n}]\!]\cdot\langle\!\langle\tilde{\mathbf{u}}^h\rangle\!\rangle+\langle\!\langle\mathbf{T}^h\mathbf{n}\rangle\!\rangle\cdot[\![\tilde{\mathbf{u}}^h]\!])\,\mathrm{d}a.\end{aligned} \tag{44}$$

Similarly, the divergence theorem applied twice yields

$$\begin{aligned}&\int_{\tilde{\mathcal{Q}}}\mathbf{G}^h:\operatorname{grad}\operatorname{curl}\tilde{\mathbf{u}}^h\,\mathrm{d}v\\&=-\int_{\tilde{\mathcal{Q}}}(\operatorname{curl}\operatorname{div}\mathbf{G}^h)\cdot\tilde{\mathbf{u}}^h\,\mathrm{d}v+\int_{\mathcal{S}}(\mathbf{G}^h\mathbf{n}\cdot\operatorname{curl}\tilde{\mathbf{u}}^h\\&\quad+(\mathbf{n}\times\operatorname{div}\mathbf{G}^h)\cdot\tilde{\mathbf{u}}^h)\,\mathrm{d}a+\int_{\tilde{\Gamma}}([\![\mathbf{G}^h\mathbf{n}]\!]\cdot\langle\!\langle\operatorname{curl}\tilde{\mathbf{u}}^h\rangle\!\rangle\\&\quad+\langle\!\langle\mathbf{G}^h\mathbf{n}\rangle\!\rangle\cdot[\![\operatorname{curl}\tilde{\mathbf{u}}^h]\!])\,\mathrm{d}a+\int_{\tilde{\Gamma}}([\![\mathbf{n}\times\operatorname{div}\mathbf{G}^h]\!]\cdot\langle\!\langle\tilde{\mathbf{u}}^h\rangle\!\rangle\\&\quad+\langle\!\langle\mathbf{n}\times\operatorname{div}\mathbf{G}^h\rangle\!\rangle\cdot[\![\tilde{\mathbf{u}}^h]\!])\,\mathrm{d}a.\end{aligned} \tag{45}$$

Here, we take advantage of the equality

$$\begin{aligned}\int_{\mathcal{S}}\mathbf{G}^h\mathbf{n}\cdot\operatorname{curl}\tilde{\mathbf{u}}^h\,\mathrm{d}a=&\int_{\mathcal{S}}\Big((\operatorname{div}_{\mathcal{S}}(\mathbf{G}^h\mathbf{n}\times)-2H\mathbf{n}\times\mathbf{G}^h\mathbf{n})\cdot\tilde{\mathbf{u}}^h\\&+(\mathbf{n}\times\mathbf{G}^h\mathbf{n})\cdot\frac{\partial\tilde{\mathbf{u}}^h}{\partial n}\Big)\,\mathrm{d}a.\end{aligned} \tag{46}$$

A detailed derivation of this equality is provided by Fried and Gurtin (2009).

The consistency of the method then follows upon substituting the results (44)–(46), into (37), viz.

$$\begin{aligned}0=&T_{cd}(\mathbf{u}^h,\tilde{\mathbf{u}}^h)-\ell_{cd}(\tilde{\mathbf{u}}^h)\\=&\int_{\tilde{\mathcal{Q}}}(\operatorname{curl}\operatorname{div}\mathbf{G}^h+\operatorname{div}\mathbf{T}^h)\cdot\tilde{\mathbf{u}}^h\,\mathrm{d}v-\int_{\tilde{\Gamma}}\langle\!\langle\tilde{\mathbf{G}}^h\mathbf{n}\rangle\!\rangle\cdot[\![\operatorname{curl}\mathbf{u}^h]\!]\,\mathrm{d}a\\&+\int_{\tilde{\mathcal{Q}}}[\![\mathbf{T}^h\mathbf{n}-\mathbf{n}\times\operatorname{div}\mathbf{G}^h+\operatorname{div}_{\mathcal{S}}(\mathbf{G}^h\mathbf{n}\times)-2H\mathbf{n}\times\mathbf{G}^h\mathbf{n}]\!]\cdot\langle\!\langle\tilde{\mathbf{u}}^h\rangle\!\rangle\,\mathrm{d}a\\&+\int_{\tilde{\mathcal{Q}}}[\![\mathbf{n}\times\mathbf{G}^h\mathbf{n}]\!]\cdot\left\langle\!\!\left\langle\frac{\partial\tilde{\mathbf{u}}^h}{\partial n}\right\rangle\!\!\right\rangle\mathrm{d}a-\int_{\mathcal{S}_{\text{free}}}(\mathbf{t}_{\mathcal{S}}-\mathbf{T}^h\mathbf{n}-\mathbf{n}\times\operatorname{div}\mathbf{G}^h\\&+\operatorname{div}_{\mathcal{S}}(\mathbf{G}^h\mathbf{n}\times)-2H\mathbf{n}\times\mathbf{G}^h\mathbf{n})\cdot\tilde{\mathbf{u}}^h\,\mathrm{d}a\\&-\int_{\mathcal{S}_{\text{free}}}(\mathbf{m}_{\mathcal{S}}+\mathbf{n}\times\mathbf{G}^h\mathbf{n})\cdot\frac{\partial\tilde{\mathbf{u}}^h}{\partial n}\,\mathrm{d}a+\tau_i\int_{\tilde{\Gamma}}[\![\operatorname{curl}\tilde{\mathbf{u}}^h]\!]\cdot[\![\operatorname{curl}\mathbf{u}^h]\!]\,\mathrm{d}a\\&+\tau_g\int_{\mathcal{I}}[\![\tilde{\mathbf{u}}^h]\!]\cdot[\![\mathbf{u}^h]\!]\,\mathrm{d}a-\mathcal{W}_{\mathcal{I}}(\mathbf{u}^h,\tilde{\mathbf{u}}^h)-\mathcal{W}_{\mathcal{J}}(\mathbf{u}^h,\tilde{\mathbf{u}}^h)-\mathcal{W}_{\partial\mathcal{J}}(\mathbf{u}^h,\tilde{\mathbf{u}}^h).\end{aligned} \tag{47}$$

From (47), we deduce the governing equations

$$\operatorname{div}\mathbf{T}^h+\operatorname{curl}\operatorname{div}\mathbf{G}^h=0\quad\text{in }\tilde{\mathcal{Q}}, \tag{48}$$

$$\left.\begin{aligned}&\mathbf{t}_{\mathcal{S}}=\mathbf{T}^h\mathbf{n}-\operatorname{div}_{\mathcal{S}}(\mathbf{G}^h\mathbf{n}\times)+\mathbf{n}\times(\operatorname{div}\mathbf{G}^h+2H\mathbf{G}^h\mathbf{n}),\\&\mathbf{m}_{\mathcal{S}}=\mathbf{G}^h\mathbf{n}\times\mathbf{n};\end{aligned}\right\}\quad\text{on }\mathcal{S}_{\text{free}}, \tag{49}$$

with interfacial conditions

$$\left.\begin{aligned}&[\![\mathbf{T}^h]\!]\mathbf{n}=\operatorname{div}_{\mathcal{S}}([\![\mathbf{G}^h]\!]\mathbf{n}\times)-2H\mathbf{n}\times[\![\mathbf{G}^h]\!]\mathbf{n}-\mathbf{n}\times\operatorname{div}[\![\mathbf{G}^h]\!],\\&\mathbf{n}\times[\![\mathbf{G}^h]\!]\mathbf{n}=\mathbf{0},\end{aligned}\right\}\quad\text{on }\mathcal{I}, \tag{50}$$

the triple-junction condition

$$\textstyle\sum_{\iota=1}^{3}(\boldsymbol{\nu}_\iota\times[\![\mathbf{G}^h]\!]\mathbf{n}_\iota)=\mathbf{0},\quad\text{on }\mathcal{J}, \tag{51}$$

the boundary-junction condition

$$\boldsymbol{\nu}\times[\![\mathbf{G}^h]\!]\mathbf{n}=-\boldsymbol{\nu}_{\mathcal{I}}\times[\![\mathbf{G}^h]\!]\mathbf{n}_{\mathcal{I}},\quad\text{on }\partial\mathcal{J}, \tag{52}$$

and jump conditions

$$\left.\begin{aligned}&[\![\operatorname{curl}\tilde{\mathbf{u}}^h]\!]=\mathbf{0},\\&[\![\mathbf{T}^h\mathbf{n}-\mathbf{n}\times\operatorname{div}\mathbf{G}^h+\operatorname{div}_{\mathcal{S}}(\mathbf{G}^h\mathbf{n}\times)-2H\mathbf{n}\times\mathbf{G}^h\mathbf{n}]\!]=\mathbf{0},\\&[\![\mathbf{n}\times\mathbf{G}^h\mathbf{n}]\!]=\mathbf{0},\end{aligned}\right\}\quad\text{on }\tilde{\Gamma}. \tag{53}$$

In the above, (48) and (49) enforce the force balance equation on the element interiors and the traction boundary conditions on free surfaces of the domain, respectively. In addition, (50)–(52) enforce the interfacial condition, the triple-junction condition, and the boundary-junction condition, respectively. Finally, $(53)_1$ ensures the continuity of the first derivatives across element boundaries, and $(53)_{2,3}$ ensure the continuity of the traction across the interelement boundaries.

4.2. Element choice for the displacement field

We establish our formulation using four-node isoparametric quadrilateral elements with piecewise-quadratic basis functions for the displacement field. To begin, we introduce the space

$$P^j(\mathcal{Q}_e)=\{\mathbf{v}:\mathbf{v}\text{ is a polynomial of degree }\leqslant j\text{ on }\mathcal{Q}_e\} \tag{54}$$

of complete polynomials over element $\mathcal{Q}_e$. Using M to denote the number of nodes in the mesh, we then write

$$\{\phi_I\}=\{\phi_I\in C^0(\mathcal{Q}^h):\phi_I|\mathcal{Q}_e\in P^2(\mathcal{Q}_e)\},\quad I=1\ldots M, \tag{55}$$

for the set of quadratic Lagrangian isoparametric functions. The approximation to the displacement field is then given by

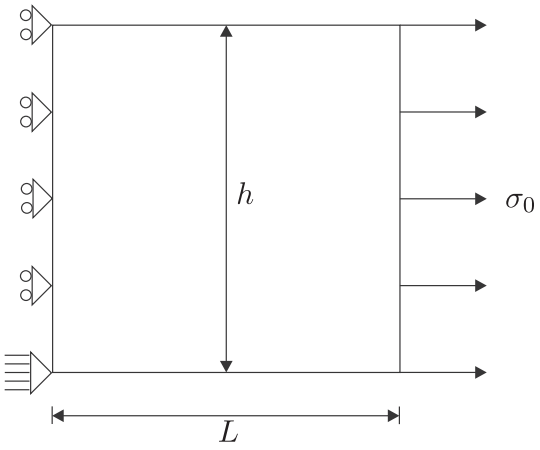

Fig. 2. Schematic of a polycrystal with displacement free to slide vertically on the left end and uniform traction σ_0 applied to the right end.

$$\mathbf{u}^h(\mathbf{x}) = \sum_{I=1}^{M} \phi_I(\boldsymbol{\xi}(\mathbf{x}))\mathbf{u}_I, \tag{56}$$

where $\mathbf{u}_I$ is the nodal value at node I and $\boldsymbol{\xi}$ the coordinates in a reference element.

To approximate the virtual displacement $\tilde{\mathbf{u}}^h$, we use expansions analogous to (56). Upon substituting these expressions into (37) and invoking the arbitrariness of the virtual function, we obtain the linear algebraic system of equations

$$\mathbf{Kd} = \mathbf{f}, \tag{57}$$

which can be solved to yield the discrete approximation $\mathbf{d}$ to the solution.

5. Numerical studies

In this section, numerical simulations designed to explore the performance of the theory are described. In particular, we investigate the elastic properties of nanocrystalline materials along with the effects of the length scale δ and interface and junction conditions across grain boundaries.

To simulate the behavior of polycrystals, we consider a two-dimensional polycrystal, shown in Fig. 2, with length L = 100 nm and height h = 100 nm and displacement free to slide vertically on the left end. The polycrystal is also subject to a uniform traction σ_0 applied to the right end. Conditions of plane stress are assumed to prevail.

5.1. Effective stress distribution for a polycrystal

To begin, we study the distribution of the effective stress for a polycrystal with the elastic modulus of $E = 1.0 \times 10^9$ and Poisson's ratio of $\nu = 0.30$. The uniform traction $\sigma_0 = 1.0 \times 10^7$ is applied to the right end of the polycrystal. The variational formulation (37) involves two stabilization parameters τ_i and τ_g. For the stabilization parameters, we take $\tau_i = \tau_g = 1.0 \times 10^{12}$.

The first structure we tested is a polycrystal with three grains as shown in Fig. 3(a). Three grains meet at a common triple-junction, at which three grain boundaries intersect. The mesh model, refined at the triple-junction, with 3944 elements is also shown in Fig. 3(b).

The plot of the stress σ_{xx}, normalized by the applied uniform traction σ_0, is displayed in Fig. 4. For comparison, the stress distribution for the polycrystal without grains is also presented in panel (a) of the figure. The stress distribution for the polycrystal without grains is uniform over the entire domain. On the other hand, the result for a polycrystal with grains in panel (b) of the figure shows a high stress concentration at the triple-junction.

Fig. 5 shows the plot of the normalized effective stress distribution for a polycrystal with eight grains and multiple triple junctions. The plot is obtained using the mesh model with 8816 elements as shown in the figure. As shown in the previous example, the result shows higher stress concentrations at triple junctions than at grain interiors and boundaries. These results indicate that our theory can describe high strain gradients in the vicinity of the grain boundaries and triple junctions for nanoscale polycrystals.

5.2. Influence of the length scale δ

We investigate the influence of the length scale $\delta = \bar{\mu}/\mu L^2$ on the effective elastic properties. To avoid confusion, we denote by E_0 and ν_0 the elastic modulus and Poisson's ratio of conventional coarsely-grained polycrystals, respectively. On the other hand, E and ν represent the effective elastic modulus and effective Poisson's ratio for nanocrystalline materials, respectively. In this section, our simulations are performed for two cases of elastic moduli $E_0 = 1.0 \times 10^5$ Pa and 1.0×10^9 Pa and Poisson's ratio $\nu_0 = 0.3$. We take $\tau_i = \tau_g = 1.0 \times 10^8$ Pa for $E_0 = 1.0 \times 10^5$ Pa and $\tau_i = \tau_g = 1.0 \times 10^{12}$ Pa for $E_0 = 1.0 \times 10^9$ Pa.

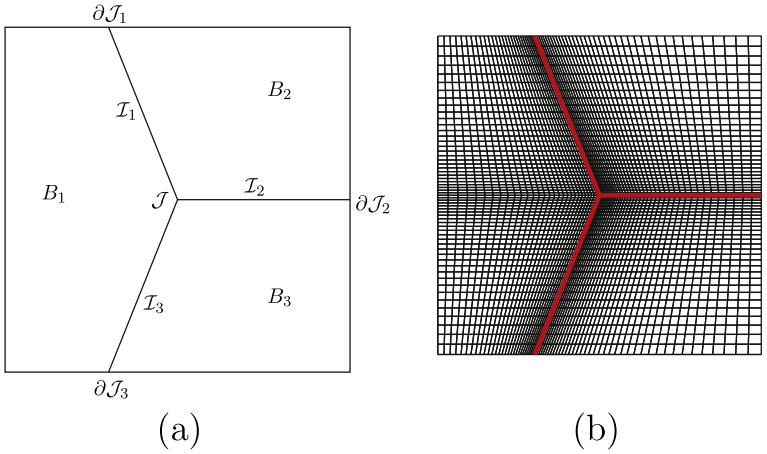

Fig. 3. (a) Schematic view of a computational domain for a polycrystal with three grains and one triple-junction. (b) The mesh model, refined at the triple-junction, with 3944 elements.

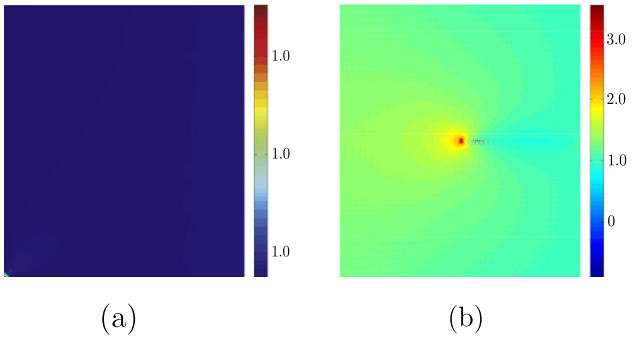

Fig. 4. Distribution of the effective stress σ_{xx}, normalized by the applied traction σ_0, for a polycrystal (a) without grains and (b) with three grains ($\delta = 4.68 \times 10^{-6}$).

As shown in Fig. 6, simulations are performed for three cases: two grains without triple junctions and eleven and twenty-three grains with multiple triple junctions. We apply uniform tractions of σ_0 ranging from 1.0×10^3 Pa to 4.0×10^3 Pa for $E_0 = 1.0 \times 10^5$ Pa and from 1.0×10^7 Pa to 4.0×10^7 Pa for $E_0 = 1.0 \times 10^9$ Pa to the right end. Recall that the theory under consideration was developed to study the elastic response of nanocrystalline materials undergoing infinitesimal deformations. Fig. 7 shows a stress–strain diagram for $E_0 = 1.0 \times 10^5$ Pa and two cases of $\delta = 1.3 \times 10^{-6}$ and 2.6×10^{-5}. Not surprisingly, the plot shows that the theory gives rise to a linear elastic relationship between stress and strain. Notice that stress–strain diagrams for other cases of δ and elastic moduli also show linear relationships. As a consequence, we obtain the effective elastic modulus E from the slope of a stress–strain curve as shown in the figure. The strain ϵ in the x-direction is computed at the right end.

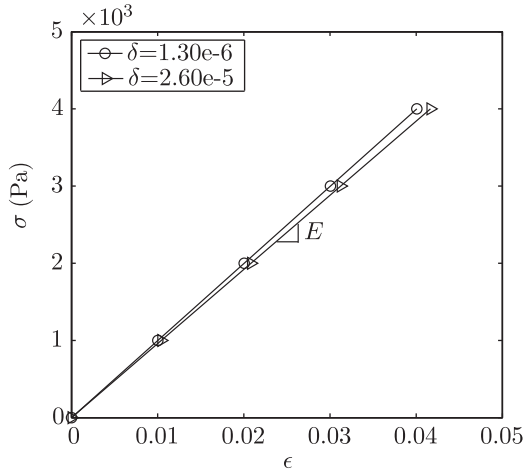

Fig. 7. A stress–strain diagram showing the linear elastic deformation for $E_0 = 1.0 \times 10^5$ Pa and the slope represents the effective elastic modulus E.

Fig. 8 shows log–log plots of the effective elastic modulus E, normalized by E_0, versus δ for $E_0 = 1.0 \times 10^5$ Pa and 1.0×10^9 Pa. Plots are provided for three cases of polycrystals shown in Fig. 6. While the effective elastic modulus decreases with increasing δ for polycrystals with triple junctions, the modulus is almost independent of a change of δ for a polycrystal without triple junctions. Both results also show that, as the number of grains increases (i.e., grain size decreases), the effective elastic modulus decreases. This is because the length scale effects and interactions across grain boundaries become significant with increasing δ and the number of grains. Importantly, as might be expected, the elastic modulus

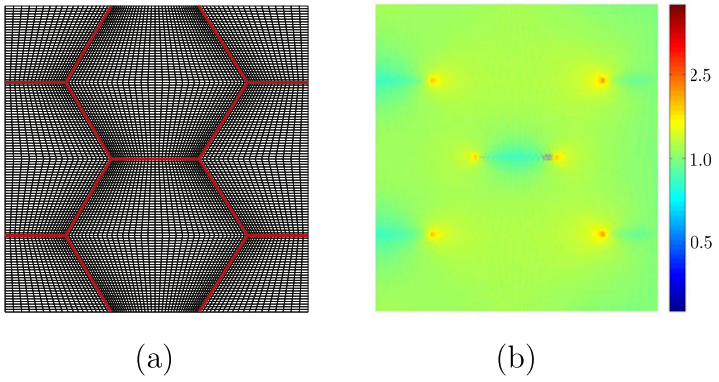

Fig. 5. (a) The mesh model, with 8816 elements, for a polycrystal with eight grains and multiple triple junctions and the red line represents grain boundaries. (b) Distribution of the effective stress σ_{xx} normalized by the applied stress σ_0 ($\delta = 1.25 \times 10^{-6}$). (For interpretation of the references to color in this figure legend, the reader is referred to the web version of this article.)

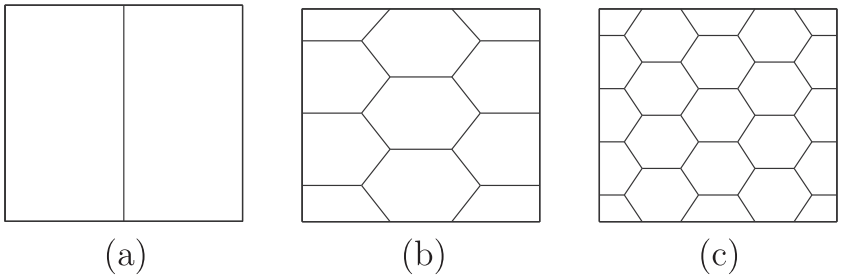

Fig. 6. Schematic of polycrystals with (a) 2 grains without triple junctions, (b) 11 grains, and (c) 23 grains.

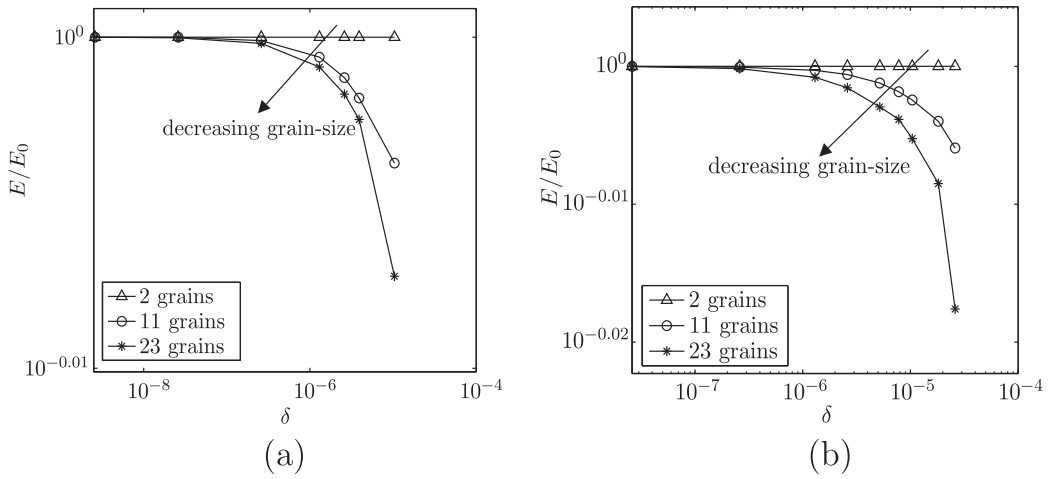

Fig. 8. Log–log plots of the effective elastic modulus E, normalized by E_0, versus δ for (a) $E_0 = 1.0 \times 10^9$ Pa and (b) $E_0 = 1.0 \times 10^5$ Pa.

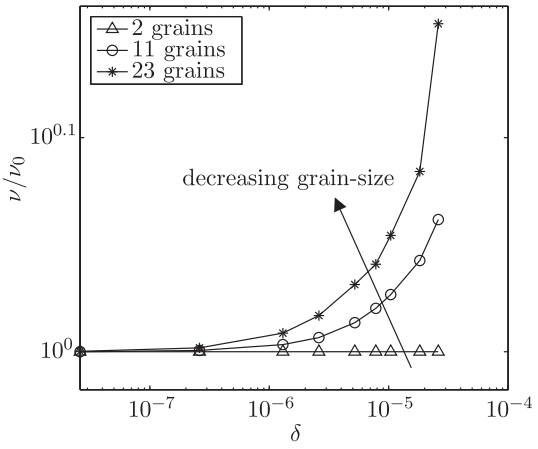

Fig. 9. A log–log plot of the effective Poisson's ratio ν, normalized by ν_0, versus δ for $E_0 = 1.0 \times 10^5$ Pa.

E_0 of the conventional grain-sized polycrystal is recovered in the limit $\delta \to 0$.

The effective Poisson's ratio ν, normalized by ν_0, versus δ is plotted in Fig. 9. Here, the effective Poisson's ratio is computed from the ratio of the lateral strain ϵ_{yy} and the axial strain ϵ_{xx} — i.e., $\nu = -\epsilon_{xx}/\epsilon_{yy}$. Interestingly, in contrast to the effective elastic modulus, the effective Poisson's ratio increases with increasing δ and the number of grains (i.e., decreasing grain size). Importantly, the effective Poisson's ratio ν reduces to Poisson's ratio ν_0 of the conventional grain-sized polycrystal in the limit $\delta \to 0$.

5.3. Effective elastic properties for nanocrystalline copper

As we mentioned in the introduction, early observations for nanocrystalline materials gave lower Young's properties than for conventional coarsely-grained polycrystals. We investigate whether our theory can predict the variation of the Young's properties with grain size for a nanocrystalline metal. The nanocrystalline material

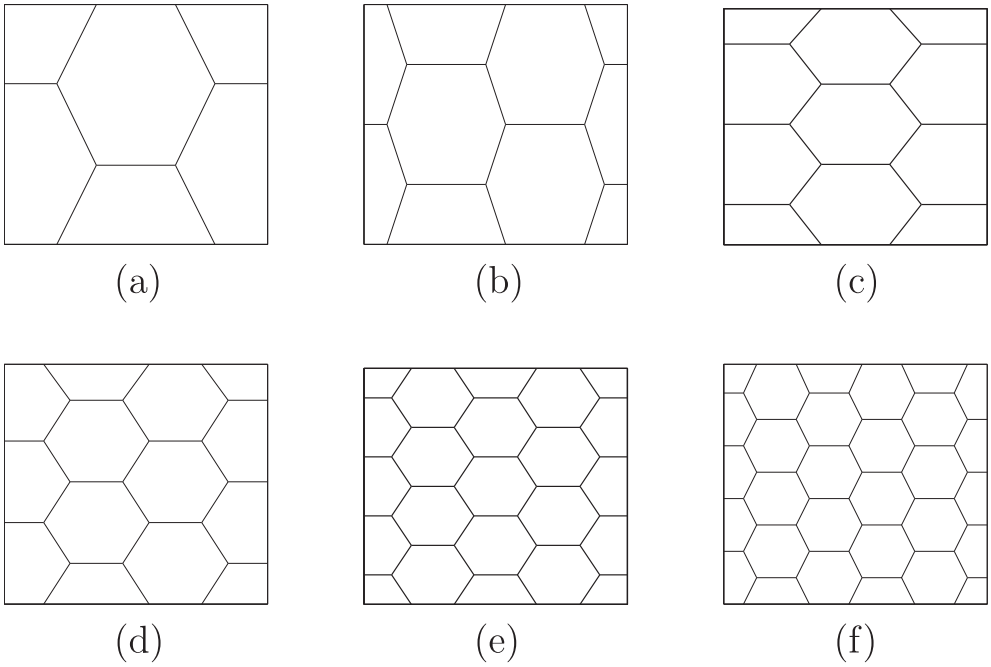

Fig. 10. Schematic of polycrystals with (a) 6 grains, (b) 10 grains, (c) 11 grains, (d) 14 grains, (e) 23 grains, and (f) 30 grains.

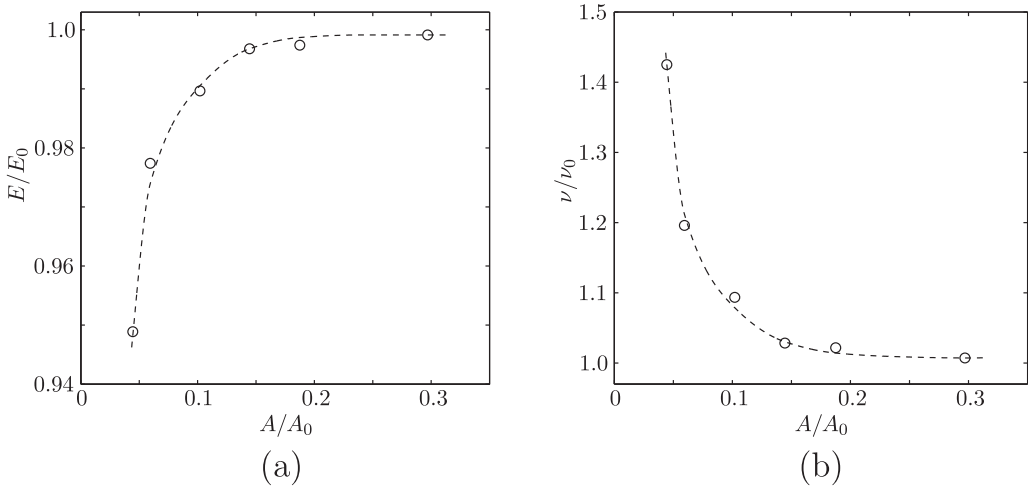

Fig. 11. Plots of the predicted variation of (a) the normalized effective elastic modulus and (b) the normalized effective Poisson's ratio with the normalized grain area A/A_0 for nanocrystalline copper.

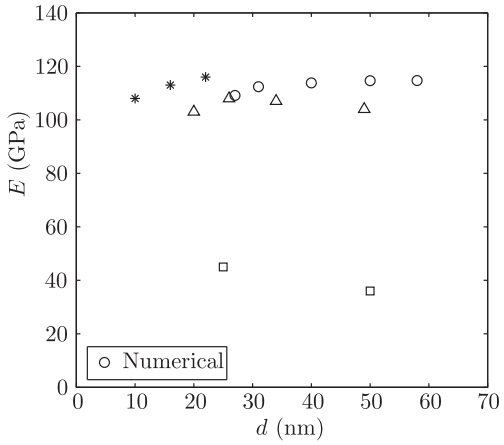

Fig. 12. Comparison of numerical results with experimental results obtained by Sanders et al. (1996) (△), Sanders et al. (1997) (∗), and Nieman et al. (1991) (□).

we used to test is copper (Cu), which, for a material with conventional grain size has Young's modulus $E_0 = 115$ GPa and Poisson's ratio $\nu_0 = 0.33$ (Sharma and Ganti, 2003; Kim et al., 1998).

We consider a polycrystal of length $L = 100$ nm and height $h = 100$ nm and take $\delta = 1.39 \times 10^{-5}$. Simulations are performed on polycrystals, displayed in Fig. 10, ranging from six grains to thirty grains. The size of grains, based on the maximum distance between edges in a grain, approximately ranges from 27 nm to 73 nm. We note that as the number of grains increases, the portion of grain boundaries and triple junctions is increased and grain size decreases.

Fig. 11 shows plots of the predicted variation of the normalized effective elastic modulus and Poisson's ratio versus grain area A, normalized by the total area A_0 (i.e., $A_0 = Lh$), for nanocrystalline copper. The effective elastic modulus reduces as the grain area decreases. In contrast to the effective elastic modulus, as grain area decreases, the effective Poisson's ratio increases. These results are reasonable, as a larger fraction of the atoms belongs to the grain boundaries and the material comprising those boundaries is softer than that of the adjacent grains. In particular, the result shows an approximate 5% reduction of the effective elastic modulus for nanocrystalline copper with a grain size of 27 nm. This result is comparable to the experimental result which shows about a 6% reduction of the elastic modulus for nanocrystalline copper with grain size of 26 nm obtained by Sanders et al. (1996) and compares favorably with the analytical results of Sharma and Ganti (2003). This finding indicates that our theory can be used to capture the reduction of the elastic moduli of nanocrystalline materials. In Fig. 12, we provide a plot of the effective elastic modulus which shows comparison of our numerical results with experimental results. Despite the simplicity of our theory, the numerical results reproduce the experimental results obtained by Sanders et al. (1996, 1997) fairly well.

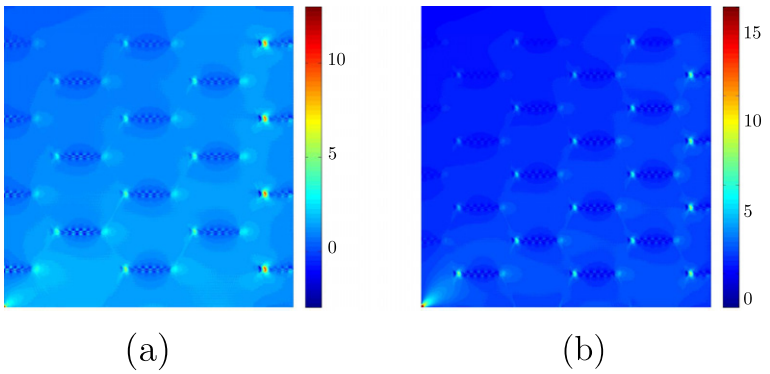

Fig. 13. Distribution of the effective stress σ_{xx}, normalized by the applied stress σ_0, for NC copper with (a) 23 grains at 14,560 elements and (b) 30 grains at 18,648 elements.

In Fig. 13, we display the distribution of the effective stress for nanocrystalline copper with twenty-three and thirty grains as shown in panels (e) and (f) in Fig. 10. Both results show high strain gradients near grain boundaries and triple junctions. These results support observations due to Maranganti and Sharma (2007), who note that "strain gradients are generally large only at nanoscale dimensions or in the vicinity of defects". In a polycrystal, grain boundaries and triple junctions represent defects at which the lattices of adjacent grains do not match.

6. Summary and conclusions

In this paper, we investigate the elastic properties of a nanoscale polycrystal based on the continuum theory introduced by Fried and Gurtin (2009). The theory gives rise to a balance equation that is fourth-order in the displacement field and incorporates interfacial conditions and junction conditions across grain boundaries. Rather than employing C^1-continuous basis functions, we present a relatively efficient finite-element method using C^0-continuous basis functions. Continuity of higher-order displacement derivatives is enforced between elements using a variation of Nitsche's (1970) method, involving jump quantities across interelement boundaries.

Using the finite-element method, we examine the capability of our theory by performing numerical simulations for a polycrystal subject to an uniaxial deformation. The distribution of the effective stress for polycrystals shows that our theory can capture large strain gradients near triple junctions and grain boundaries. We also study the influence of the gradient length scale δ, which represents the length scale effect at the nanoscale. As δ increases, the effective Young's modulus decreases and Poisson's ratio increases. Importantly, the effective elastic modulus and the effective Poisson's ratio reduce to Young's modulus and Poisson's ratio of conventional grain-sized polycrystal in the limit $\delta \to 0$. Of particular interest is the observation that our theory captures lower Young's modulus for bulk nanocrystalline materials than for conventional coarsely-grained polycrystals. The result shows about a 5% reduction of the effective elastic modulus for nanocrystalline copper and it compares favorably with experimental results.

The non-conforming method we have developed includes parameters τ_i and τ_g to stabilize higher-order derivatives across interelement boundaries and the displacement field at grain boundaries. The accuracy depends on the choice of these stabilization parameters. To overcome this drawback, we intend to develop a more robust algorithm based on the variational multiscale method in which the fine-scale bulk field is approximated with higher-order edge-bubbles. This approach will provide static condensation and eliminate the stabilization parameters. Along these lines, Kim and Dolbow (2009) have recently developed an edge-bubble stabilized finite-element method for fourth-order parabolic problems that stabilization parameters follow automatically from the approximation to the fine scale.

Fried and Gurtin (2009) provided constitutive relations with both isotropic and cubic parts of the stress **T** and the hyperstress **G**. Our current work neglects the cubic part of the stresses. Future work will explore the impact of anisotropy. Our current studies are performed for nanocrystalline materials consisting of grains of equiaxed shape, in which all characteristics of grain size are of the same order. In the future, we plan to study nanocrystalline materials with columnar and other nonequiaxed geometries.

References

Annavarapu, C., Hautefeuille, M., Dolbow, J.E., 2012. A robust Nitsche's formulation for interface problems. Comput. Methods Appl. Mech. Eng. 225–228, 44–54.

Babuška, I., 1973. The finite element method with penalty. Math. Comput. 27, 221–228.

Baumann, C.E., 1997. The hp-adaptive discontinuous finite element method for computational fluid dynamics. Ph.D. Thesis, The University of Texas at Austin, Austin, TX.

Bush, M.B., 1993. Modelling of nanophase materials. Mater. Sci. Eng. A 16, 127–134.

Dao, M., Lu, L., Asaro, R.J., De Hosson, J.T.M., Ma, E., 2005. Toward a quantitative understanding of mechanical behavior of nanocrystalline metals. Acta Mater. 55, 4041–4065.

Douglas, J., Dupont, T., 1976. Interior penalty procedures for elliptic and parabolic Galerkin methods. In: Computing Methods in Applied Sciences. Lecture notes in Physics, vol. 58. Springer-Verlag, Berlin.

Engel, G., Garikipati, K., Hughes, T.J.R., Larson, M.G., Mazzei, L., Taylor, R.L., 2002. Continuous/Discontinuous finite element approximations of fourth-order elliptic problems in structural and continuum mechanics with applications to thin beams and plates, and strain gradient elasticity. Comput. Methods Appl. Mech. Eng. 191, 3669–3750.

Fortin, M., Brezzi, F., 1991. Mixed and Hybrid Finite Element Methods. Springer, New York.

Fougere, G., Riester, L., Ferber, M., Weertman, J., Siegel, R., 1995. Young's modulus of nanocrystalline Fe measured by nanoindentation. Mater. Sci. Eng. A 204, 1–6.

Fried, E., Gurtin, M.E., 2009. Gradient nanoscale polycrystalline elasticity: intergrain interactions and triple-junction conditions. J. Mech. Phys. Solids 57, 1749–1779.

Gallas, M.R., Piermarini, G.J., 1991. Bulk modulus and Young's modulus of nanocrystalline γ-alumina. J. Am. Ceram. Soc. 77, 2917–2920.

Gleiter, H., 1989. Nanocrystalline materials. Prog. Mater. Sci. 33, 223–315.

Gleiter, H., 2000. Nanostructured materials: basic concepts and microstructure. Acta Mater. 48, 1–29.

Griebel, M., Schweitzer, M.A., 2002. A particle-partition of unity method. Part V: boundary conditions. In: Hildebrandt, S., Karcher, H. (Eds.), Geometric Analysis and Nonlinear Partial Differential Equations. Springer-Verlag, Berlin, pp. 519–542.

Gurtin, M.E., 2001. A gradient theory of single-crystal viscoplasticity that accounts for geometrically necessary dislocations. J. Mech. Phys. Solids 84, 809–819.

Han, B.Q., Lavernia, E.J., Mohamed, F.A., 2005. Mechanical properties of nanostructured materials. Rev. Adv. Mater. Sci. 9, 1–16.

Hasnaoui, A., Van Swygenhoven, H., Derlet, P.M., 2003. Dimples on nanocrystalline fracture surfaces as evidence for shear plane formation. Science 300, 1550–1552.

Hughes, T.J.R., Cottrell, J.A., Bazilevs, Y., 2005. Isogeometric analysis: CAD, finite elements, NURBS, exact geometry and mesh refinement. Comput. Methods Appl. Mech. Eng. 194, 4135–4195.

Kim, H.S., Bush, M.B., 1999. The effects of grain size and porosity on the elastic modulus of nanocrystalline materials. Nanostruct. Mater. 11, 361–367.

Kim, T.-Y., Dolbow, J.E., 2009. An edge-bubble stabilized finite element method for fourth-order parabolic problems. Finite Elem. Anal. Des. 45, 485–494.

Kim, H.S., Suryanarayana, C., Kim, S.J., Chun, B.S., 1998. Numerical investigation of mechanical behavior of nanocrystalline copper. Powder Metall. 41, 217–220.

Kim, T.-Y., Dolbow, J.E., Fried, E., 2007. A numerical method for a second-gradient theory of incompressible fluid flow. J. Comput. Phys. 223, 551–570.

Koch, C.C., 2007. Structural nanocrystalline materials: an overview. J. Mater. Sci. 42, 1403–1414.

Krstic, V., Erb, U., Palumbo, G., 1993. Effect of porosity on Young's modulus of nanocrystalline materials. Scr. Metall. Mater. 29, 1501–1504.

Kumar, K.S., Swygenhoven, H.V., Suresh, S., 2003. Mechanical behavior of nanocrystalline metals and alloys. Acta Mater. 51, 5743–5774.

Maranganti, R., Sharma, P., 2007. Length scales at which classical elasticity breaks down for various materials. Phys. Rev. Lett. 94, 195504.

Meyers, M.A., Mishra, A., Benson, D.J., 2006. Mechanical properties of nanocrystalline materials. Prog. Mater. Sci. 51, 427–556.

Nieman, G.W., Weertman, J.R., Siegel, R.W., 1991. Mechanical behavior of nanocrystalline Cu and Pd. J. Mater. Res. 6, 1012–1027.

Nitsche, J.A., 1970. Über ein Variationsprinzip zur Lösung von Dirichlet-Problemen bei Verwendung von Teilräumen, die keinen Randbedingungen unterworfen sind. Abh. Math. Sem. Hamburg 36, 9–15.

Petera, J., Pittman, J.F.T., 1994. Isoparametric Hermite elements. Int. J. Numer. Methods Eng. 37, 3489–3519.

Ramesh, K.T., 2009. Nanomaterials, Mechanics and Mechanisms. Springer, Dordrecht, Heidelberg, London, and New York.

Sanders, P.G., Eastman, J.A., Weertman, J.R., 1996. Tensile behavior of nanocrystalline copper. In: Suryanarayana, C., Singh, J., Froes, F.H. (Eds.), Processing and Properties of Nanocrystalline Materials. The Minerals, Metals & Materials Society, pp. 379–386.

Sanders, P.G., Eastman, J.A., Weertman, J.R., 1997. Elastic and tensile behavior of nanocrystalline copper and palladium. Acta Mater. 45, 4019–4025.

Schiotz, J., Vegge, T., Di Tolla, D., Jacobsen, K., 1999. Atomic-scale simulations of the mechanical deformation of nanocrystalline metals. Phys. Rev. B (Condensed Matter and Materials Physics) 60, 971–983.

Sharma, P., Ganti, S., 2003. On the grain-size-dependent elastic modulus of nanocrystalline materials with and without grain-boundary sliding. J. Mater. Res. 18, 1823–1826.

Shen, T.D., Koch, C.C., Tsui, T.Y., Pharr, G.M., 1995. On the elastic moduli of nanocrystalline Fe, Cu, Ni, and Cu–Ni alloys prepared by mechanical milling/alloying. J. Mater. Res. 10, 2892–2896.

Siegel, R.W., 1991. Cluster-assembled nanophase materials. Nanostruct. Mater. 21, 559–578.

Suryanarayana, C., Koch, C.C., 2000. Nanocrystalline materials: current research and future directions. Hyperfine Interact. 130, 5–44.
Tanimoto, H., Sakai, S., Mizubayashi, H., 1999. Mechanical behavior of high-density nanocrystalline gold prepared by gas deposition method. Nanostruct. Mater. 12, 751–756.
Tjong, S.C., Chen, H., 2004. Nanocrystalline materials and coatings. Mater. Sci. Eng. R 45, 1–88.
Van Swygenhoven, H., Derlet, P.M., 2001. Grain-boundary sliding in nanocrystalline fcc metals. Phys. Rev. B 64, 224105–224109.
Wriggers, P., Zavarise, G., 2008. A formulation for frictionless contact problems using a weak form introduced by Nitsche. Comput. Mech. 41, 407–420.
Yeheskel, O., Shen, Z., Nygren, M., 2005. Elastic moduli of grain boundaries in nanocrystalline MgO ceramics. J. Mater. Res. 20, 719–725.